npj | energy materials

Article

https://doi.org/10.1038/s44456-026-00013-5

Unraveling vacancy-modulated proton transport beyond trapping in partially hydrated Y-doped $BaZrO_3$ using a charge-aware foundation potential

Sooraj Patel[1], Anvesh Nathani[1], Jiachen Li[2], Shuanglin Zheng[1], Dengke Chen[2], Hanping Ding[1], Pejman Kazempoor[1], Yingtao Liu[1], Fan Liu[3], Shuozhi Xu[1] & Iman Ghamarian[1] ✉

Proton transport in yttrium-doped $BaZrO_3$ is widely interpreted through dopant-associated trapping models derived from fully hydrated lattices. However, protonic ceramic electrochemical cells operate under partial hydration, where oxygen vacancies remain intrinsic to the defect chemistry and may fundamentally alter the local transport landscape. The effect of vacancy-dopant configuration on proton trapping under operating-relevant conditions remains unresolved. In the present work, proton migration in partially hydrated $Ba(Zr_{0.8}Y_{0.2})O_{3-\delta}$ is examined by explicitly resolving the placement of vacancies within Y-Y-coordinated environments. Charge-aware foundation-potential atomistics, combined with climbing-image nudged-elastic-band calculations, quantify migration barriers and thermodynamic asymmetry for all symmetry-allowed nearest-neighbor proton hops. While fully hydrated Y-Y coordination exhibits pronounced trapping characterized by asymmetric transition states and facile back-hopping, partial hydration qualitatively alters the transport regime. A vacancy positioned between two Y dopants is thermodynamically favored and remains unoccupied by protons due to unfavorable hydroxyl migration. Instead, cooperative electrostatic stabilization and lattice relaxation enable low-barrier, nearly symmetric interoctahedral proton migration across all symmetry-allowed pathways. These findings demonstrate that proton mobility under operating partial hydration is governed by vacancy configuration rather than dopant proximity alone, providing mechanistic guidance for designing high-conductivity protonic ceramics.

Proton-conducting perovskites enable efficient proton transport at intermediate temperatures, and are widely used as electrolytes, membranes, and functional components in electrochemical energy, sensing, and catalytic systems[1–5]. Within this class, barium zirconate-based perovskites are particularly attractive due to their exceptional chemical stability in humid and CO_2-containing environments[6–8]. In such materials, their macroscopic proton conductivity is governed primarily by point defect equilibria and defect interactions[9–12]. Y-doped $BaZrO_3$ (BZY) is a widely studied proton-conducting oxide in which acceptor doping increases proton concentration under humid conditions, while simultaneously introducing electrostatic and elastic distortions that modify proton site energetics[13,14]. Consequently, proton mobility is often constrained by dopant-associated trapping[15] and by complex defect interactions that arise under operating temperatures where multiple charged species coexist[16,17]. In BZY, the operative defect chemistry is defined by the acceptor doping, oxygen-vacancy formation, and hydration[18–21]. This equilibrium is commonly written as

$$H_2O + V_O^{\cdot\cdot} + O_O^{\times} \rightleftharpoons 2OH_O^{\cdot} \quad (1)$$

High p_{H_2O} promotes hydration according to Eq. (1) at low to moderate temperatures, but thermogravimetric and transport measurements show that full hydration is not sustained at elevated temperatures used in

[1]School of Aerospace and Mechanical Engineering, The University of Oklahoma, Norman, OK, USA. [2]Department of Engineering Mechanics, School of Ocean and Civil Engineering, Shanghai Jiao Tong University, Shanghai, China. [3]John and Willie Leone Family Department of Energy and Mineral Engineering, The Pennsylvania State University, University Park, PA, USA. ✉e-mail: iman@ou.edu

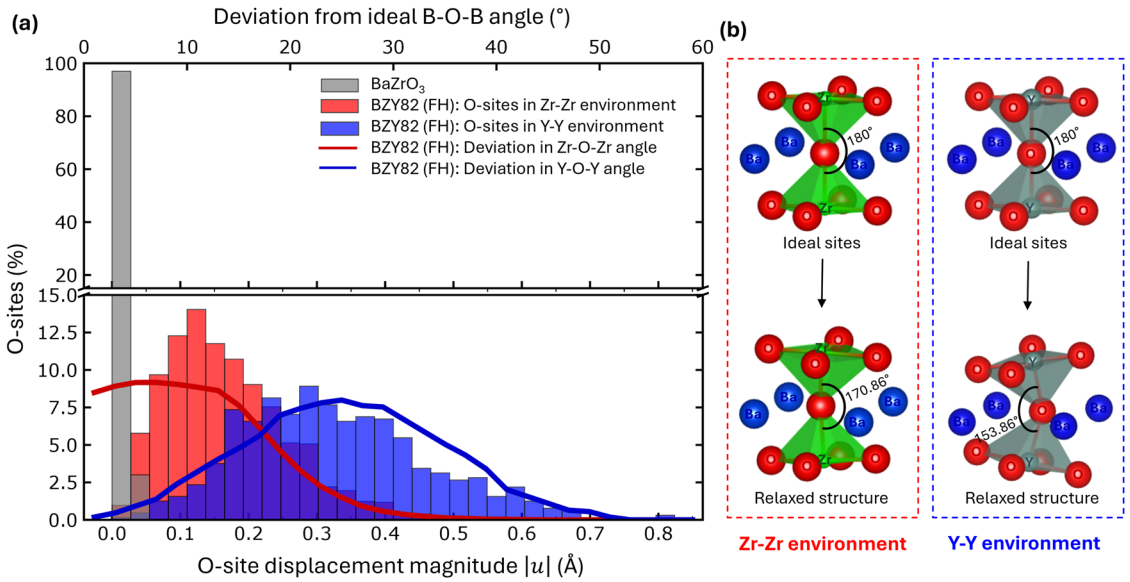

Fig. 1 | Local lattice distortion and bond-angle deviation in FH BZY82 compared with undoped $BaZrO_3$. a Distribution of oxygen-site displacement magnitude |u| referenced to the ideal cubic lattice. **b** Representative structural schematics of the ideal and relaxed configurations of BZY82 for the Zr-Zr and Y-Y environments. The Y-Y environment exhibits a broader oxygen displacement distribution accompanied by a larger angular deviation, reflecting enhanced octahedral tilting and lattice distortion relative to the Zr-Zr environment.

electrochemical cell operation[22,23]. Protons and oxygen vacancies coexist over a broad range of p_{H_2O} and temperature[24]. This partially hydrated (PH) state impacts proton transport[25,26]. Vacancy-containing environments modify local electrostatics through the exposed dopant charge and vacancy compensation. They also change oxygen-sublattice relaxations and defect-driven lattice strain[13]. These effects shift proton site energies and can alter the rate-limiting step for long-range conduction[27]. First-principles thermodynamic studies show that proton uptake is controlled by hydration thermodynamics and entropic contributions[23,28]. These finite-temperature effects can significantly alter the equilibrium populations of defects.

Proton trapping is a primary limitation of proton mobility in acceptor-doped electrolytes[15]. It arises from dopant-associated stabilization of protonic defects and is therefore governed by dopant proximity and the local dopant arrangement[29]. In BZY, agglomerated Y-Y coordination forms deep binding sites that induce thermodynamic asymmetry and suppress long-range transport, providing a stringent environment for evaluating migration and trapping behavior[30–32]. Percolation transport models further indicate that rapid conduction can be maintained through connected low-energy pathways even when protons remain preferentially associated with dopants[14]. Oxygen affinity has been proposed as a descriptor for predicting conductivity trends in doped barium zirconates by linking hydration thermodynamics to defect-association energetics[33]. Defect-sensitive probes, such as positron annihilation lifetime spectroscopy, provide complementary access to trapping-related defect populations[34]. These results highlight that trapping behavior depends on defect topology and the operative defect chemistry, particularly when oxygen vacancies remain present under incomplete hydration.

Despite these advances, proton trapping in BZY is still interpreted primarily in terms of fully hydrated (FH) or near-vacancy-free models, implicitly assuming that dopant proximity alone governs trapping. This assumption is inconsistent with electrochemical cell operating temperatures, where full hydration cannot be sustained, and oxygen vacancies remain intrinsic to the defect chemistry[22]. Under partial hydration, long-range ionic transport in BZY cannot be described by proton hopping alone. Oxygen vacancy and hydroxyl-defect migration can become kinetically competitive, particularly near dopant clusters, where defect association and oxygen-sublattice distortion are most pronounced[35,36]. Importantly, when oxygen vacancies remain associated with dopant clusters under partial hydration, proton trapping cannot be assumed a priori, as vacancy placement may remove proton-accessible binding sites and qualitatively alter the local transport topology. In addition, oxygen-sublattice distortion breaks the equivalence of nominally symmetry-related proton hops. This produces barrier dispersion and transition-state asymmetry that cannot be captured by sampling a single pathway. A rigorous trapping assessment requires systematic sampling across all nearest-neighbor hops and separation of distortion-driven asymmetry from vacancy-induced electrostatic bias. This gap motivates an explicit evaluation of proton migration and trapping in PH BZY across controlled vacancy and dopant configurations.

In the present work, we evaluate proton migration and trapping in PH BZY by explicitly resolving vacancy topology within Y-Y environments and its impact on the local migration landscape. Charge-aware foundation potential-based atomistics combined with climbing-image nudged-elastic band (CI-NEB) calculations are used to quantify migration barriers and thermodynamic asymmetry across all eight nearest-neighbor proton hops in targeted local chemistries. The approach is first validated by reproducing systematic proton trapping in Y-Y coordination under full hydration. The analysis is then extended to PH configurations, where proton hopping is compared with oxygen vacancy and hydroxyl-defect migration to assess competing activated pathways. Finally, the role of vacancy placement within Y-Y motifs is isolated, revealing that a vacancy between two Y dopants avoids conventional trapping signatures and enables low-barrier inter-octahedral transport across all accessible hop geometries. These results establish vacancy topology as a controlling factor for proton transport beyond classical trapping behavior in PH Y-doped $BaZrO_3$.

Results

Local structural distortion

The structural state of the oxygen-sublattice provides the baseline for interpreting proton migration in both undoped and Y-doped $BaZrO_3$. Deviations of oxygen positions from the ideal cubic perovskite lattice were quantified using the scalar displacement descriptor $|u|$, computed after optimal lattice alignment of fully relaxed structures. Site-resolved classification of oxygen environments was performed based on local dopant coordination, and the statistical decomposition of $|u|$ is provided in Supplementary Note S1. The corresponding probability distributions and B-O-B bond-angle distributions are shown in Fig. 1. The schematics show

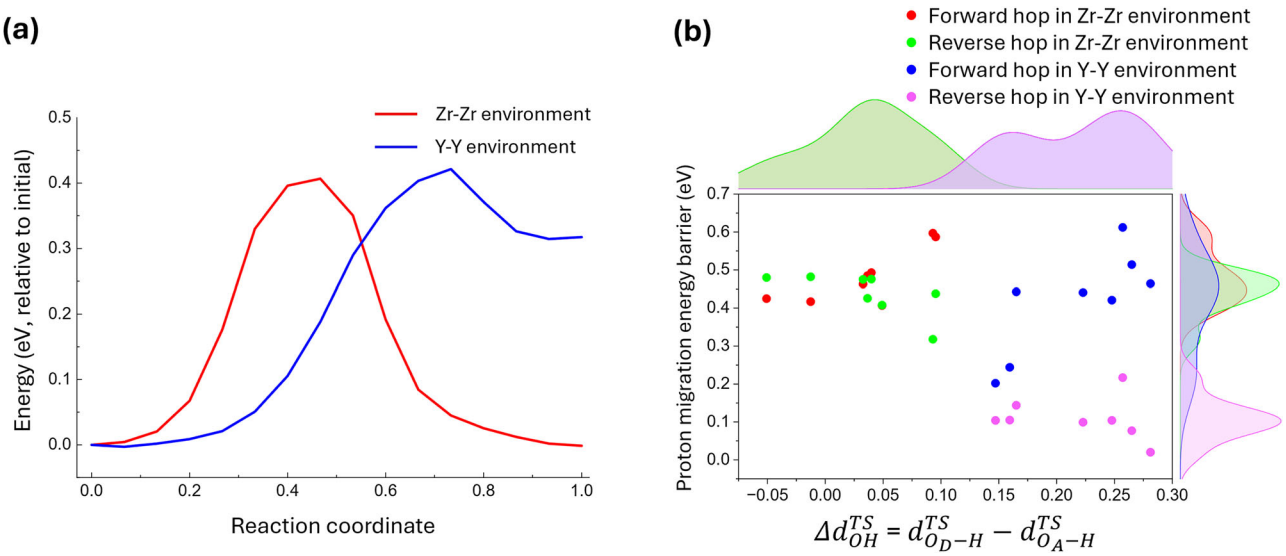

Fig. 2 | Y-Y coordination produces asymmetric proton migration and a trapping signature. a Minimum-energy profiles for proton hop in the FH Zr-Zr and Y-Y environments. Energies are referenced to the initial state of each hop. The Zr-Zr environment exhibits comparable end-state energies, whereas the Y-Y environment shows thermodynamic bias toward the Y-Y centered oxygen-site. **b** Relationship between transition-state proton-sharing asymmetry (Δd_{OH}^{TS}) and migration barriers for forward and reverse hops in the Zr-Zr and Y-Y environments.

localized relaxation and B-O-B angle in representative relaxed structures within Zr-Zr and Y-Y environments.

BZY82 exhibits a broadened oxygen displacement distribution relative to undoped $BaZrO_3$, indicating dopant-induced distortion of the oxygen sublattice. Oxygen sites in the Y-Y environment show larger displacement magnitudes and a pronounced high-$|u|$ tail compared with Zr-Zr sites. A consistent trend is observed in the angular distortion: the Y-O-Y environment exhibits a broader distribution and larger deviation from the ideal 180° B-O-B angle than the Zr-O-Zr environment. These results indicate enhanced octahedral tilting and anisotropic lattice relaxation around Y-rich local coordination environments. A consistent trend is observed for PH configurations, as detailed in Supplementary Note S1.

These observations demonstrate that Y-doping and hydration induce spatially extended distortions of the oxygen sublattice in BZY82, resulting in a heterogeneous elastic network rather than localized defect-driven perturbations. As proton migration proceeds through O-O hopping pathways that are highly sensitive to local lattice geometry and compliance, pre-existing lattice strain leads to spatial variability in proton migration barriers across distinct local chemical environments[37]. The following section examines the roles of structural heterogeneity, dopant-induced electrostatic interactions, and local defect configurations in breaking oxygen-sublattice symmetry and governing the observed variations in migration barriers.

Fully hydrated BZY82

This section establishes the baseline proton migration behavior in fully hydrated BZY82 by systematically resolving hop-specific energetics under controlled local B-site coordination environments. The objective is to isolate dopant-induced electrostatic and structural effects on proton trapping before introducing vacancy-mediated perturbations under partial hydration.

A comparative assessment of multiple foundation potentials for proton migration and the rationale for selecting the QET model are provided in Supplementary Note S2. In undoped $BaZrO_3$, the QET foundation potential predicts a proton migration barrier of 0.466 eV, consistent with prior density functional theory (0.48 eV)[37] and empirical valence-bond molecular-dynamics studies (0.42 eV)[38]. This value serves as a reference for evaluating dopant-induced perturbations in Y-doped systems. In FH BZY82, proton migration was examined under two local B-site coordination environments: (i) a Zr-Zr environment, representing weakly dopant-perturbed coordination, and (ii) a Y-Y environment, representing strongly dopant-perturbed coordination, as illustrated in a representative schematic of the relaxed local structures (Fig. 1(b)). For each environment, migration barriers were computed for all eight nearest-neighbor O-O hopping pathways originating from a common donor site (O_0).

Figure 2(a) shows minimum-energy profiles for proton migration in the FH Zr-Zr and Y-Y environments for the O_0-O_7 hop, while the complete hop-resolved pathways for all symmetry-allowed hops are provided in Supplementary Notes S3.1 and S3.2. The corresponding numerical barriers for all hops are summarized in Table 1. In the Zr-Zr environment, forward migration barriers range from 0.407 to 0.597 eV, with an average of 0.484 ± 0.073 eV, which closely resembles the barrier of undoped $BaZrO_3$. Forward and reverse barriers are comparable for all hops, indicating that the initial and final states are energetically equivalent between equivalent oxygen sites. In contrast, the Y-Y environment exhibits a broader distribution of forward barriers, ranging from 0.202 to 0.612 eV, with an average value of 0.418 ± 0.132 eV. Reverse barriers are systematically lower, averaging 0.109 ± 0.06 eV, indicating a pronounced thermodynamic asymmetry between the initial and final states. Complete hop-resolved minimum-energy pathways, donor-acceptor separation profiles, and transition-state structural descriptors for all eight symmetry-allowed hops in the Zr-Zr and Y-Y environments are provided in Supplementary Notes S3.1 and S3.2, respectively. The proton hop in the Y-Y environment shows a pronounced proton-sharing asymmetry, as shown in Fig. 2(b) and further discussed in the Discussion. Proton hop in the Zr-Y environment was also examined and showed nearly symmetric forward and reverse barriers, indicating no pronounced trapping signature for the selected isolated Zr-Y pathway (Supplementary Note S3.3).

As protonic ceramic electrochemical cells operate above 500 °C, full hydration cannot be maintained, and oxygen vacancies persist as an intrinsic component of the operating conditions[24,33,39]. In addition to Grotthuss-type proton transfer, previous studies have reported the possibility of vehicle-type hydroxyl-defect diffusion in the presence of oxygen vacancies[40–43]. To assess the relative mobility of these species in the context of structural distortion, migration barriers for oxygen vacancies, hydroxyls, and protons were evaluated for all symmetrically allowed migrations in both Zr-Zr and Y-Y local environments.

Table 1 | Proton migration barriers and transition-state structural descriptors for all eight nearest-neighbor O-O hops from O_0 in FH BZY82 under Zr-Zr and Y-Y nearest B-site environments

Hop	Zr-Zr environment				Y-Y environment			
	$\Delta E^{forward}$ (eV)	$\Delta E^{reverse}$ (eV)	$\theta_{initial}$ (Zr-O_0-Zr) (°)	Δd_{OH}^{TS} (Å)	$\Delta E^{forward}$ (eV)	$\Delta E^{reverse}$ (eV)	$\theta_{initial}$ (Y-O_0-Y) (°)	Δd_{OH}^{TS} (Å)
O_0-O_1	0.597	0.318	169.792	0.093	0.464	0.020	161.166	0.281
O_0-O_2	0.463	0.475	173.965	0.033	0.202	0.104	154.620	0.147
O_0-O_3	0.587	0.438	173.012	0.095	0.612	0.217	162.451	0.257
O_0-O_4	0.417	0.482	177.051	-0.013	0.441	0.099	161.858	0.223
O_0-O_5	0.425	0.480	169.757	-0.051	0.443	0.144	161.169	0.165
O_0-O_6	0.493	0.476	174.325	0.040	0.244	0.105	154.620	0.159
O_0-O_7	0.407	0.408	172.992	0.049	0.421	0.104	162.450	0.248
O_0-O_8	0.485	0.426	177.233	0.037	0.514	0.077	161.926	0.265
Average	0.484	0.438	173.516	0.035	0.418	0.109	160.033	0.219

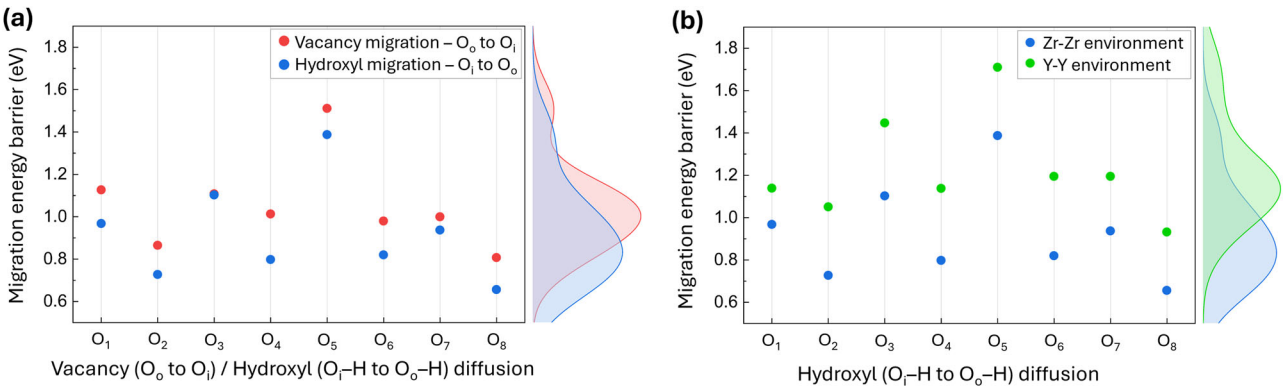

Fig. 3 | Vacancy migration is less favorable than hydroxyl migration, while Y-Y coordination further raises hydroxyl barriers. a Oxygen vacancy and hydroxyl migration barriers along symmetrically allowed pathways ($O_0 \rightarrow O_i$, i = 1 to 8) in the Zr-Zr environment, (**b**) Comparison of hydroxyl migration barriers in Zr-Zr and Y-Y environments.

Oxygen vacancy and hydroxyl migration

Figure 3a compares vacancy and hydroxyl diffusion along symmetrically allowed O_0-O_i pathways in the Zr-Zr environment. For all symmetry-allowed hops, both vacancies and hydroxyl migration barriers exhibit substantial variability. Hydroxyl diffusion consistently exhibits lower migration barriers than oxygen-vacancy diffusion. However, the average hydroxyl migration barrier in the Zr-Zr environment remains relatively high at 0.924 ± 0.235 eV. Hop-resolved oxygen vacancy and hydroxyl migration pathways are provided in Supplementary Notes S5 and S6, respectively.

Figure 3b compares hydroxyl migration barriers in Zr-Zr and Y-Y environments. In the Y-Y environment, hydroxyl migration barriers are systematically increased, with an average value of 1.225 ± 0.248 eV. Vacancy diffusion in the Y-Y environment shows even higher barriers, as detailed in Supplementary Note S5. Notably, diffusion away from a $Y'_{Zr} - \ddot{V}_O - Y'_{Zr}$ configuration exhibits an average barrier of 1.327 ± 0.211 eV, whereas the reverse diffusion toward this configuration is significantly lower (0.597 ± 0.104 eV), resulting in a substantial energy difference between end states (0.731 ± 0.287 eV).

Proton migration in partially hydrated BZY82

Under partial hydration, proton migration is governed by local vacancy-dopant coordination. Accordingly, proton transport is examined in both Zr-Zr and Y-Y environments for configurations in which an oxygen vacancy is either adjacent to one Y dopant or located between two Y dopants. The Zr-Zr environment serves as a reference for separating vacancy-induced effects from dopant-associated effects.

First, we considered the configuration in which the oxygen vacancy is positioned at the O_1 site, adjacent to one of the Y dopants in the Y-Y environment. Migration barriers for proton hops are summarized in Table 2, with full pathway details provided in Supplementary Note S7. In the Zr-Zr environment, despite negligible changes in donor–acceptor separation at the initial state and transition state, the average proton migration barrier increases to 0.511 ± 0.08 eV compared with the FH case.

In the Y-Y environment with the vacancy at O_1, the combined presence of a vacancy, a proton, and two Y dopants produces a broad distribution of proton migration barriers. The forward migration barriers span a wide range from 0.306 to 0.689 eV, with an average value of 0.471 ± 0.13 eV. Figure 4(a) shows representative proton migration profiles for the O_0-O_5 and O_0-O_7 hops in the PH Y-Y environment with a vacancy at O_1. These two pathways were selected because they illustrate the contrasting vacancy-modulated migration behavior discussed below, while the complete hop-resolved profiles are provided in Supplementary Note S7.2. For most Y-Y hops, the reverse barriers remain lower, consistent with the trapping behavior observed in the FH Y-Y environment. Notably, the O_0-O_3 and O_0-O_7 hops deviate from this trend and exhibit significantly higher reverse barriers of 0.574 and 0.547 eV, respectively (Table 2).

We then examined the second vacancy topology, in which the oxygen vacancy is located at the O_0 site between two Y dopants. This vacancy-centered Y-Y configuration is energetically stabilized (Supplementary Note S4), consistent with local electrostatic compensation between the positively charged oxygen vacancy and the negatively charged acceptor dopants. Proton migration barriers were evaluated for interoctahedral hops, specifically O_1-O_5, O_2-O_6, O_3-O_7, and O_4-O_8. The corresponding structural descriptors and migration barriers are summarized in Table 3. For comparison, analogous interoctahedral hops were examined in the Zr-Zr environment.

Table 2 | Proton migration barriers and transition-state structural descriptors for nearest-neighbor hops from O_0 in PH BZY82, with the vacancy located at the O_1 site, under Zr-Zr and Y-Y nearest B-site environments

Hop	Zr-Zr environment				Y-Y environment			
	$\Delta E^{forward}$ (eV)	$\Delta E^{reverse}$ (eV)	$\theta_{initial}$ (Zr-O_0-Zr) (°)	Δd_{OH}^{TS} (Å)	$\Delta E^{forward}$ (eV)	$\Delta E^{reverse}$ (eV)	$\theta_{initial}$ (Y-O_0-Y) (°)	Δd_{OH}^{TS} (Å)
O_0-O_2	0.508	0.548	162.152	0.008	0.347	0.216	146.104	0.165
O_0-O_3	-	-	-	-	0.689	0.574	159.093	0.200
O_0-O_4	0.565	0.592	161.574	0.002	0.419	0.242	146.105	0.164
O_0-O_5	0.525	0.311	166.366	0.103	0.306	0.054	136.277	0.253
O_0-O_6	0.585	0.487	162.193	0.075	0.558	0.236	146.140	0.191
O_0-O_7	0.502	0.587	170.182	0.045	0.471	0.547	159.520	0.192
O_0-O_8	0.509	0.419	161.574	0.092	0.504	0.169	146.104	0.220
Average	0.532	0.491	164.007	0.054	0.471	0.291	148.478	0.198

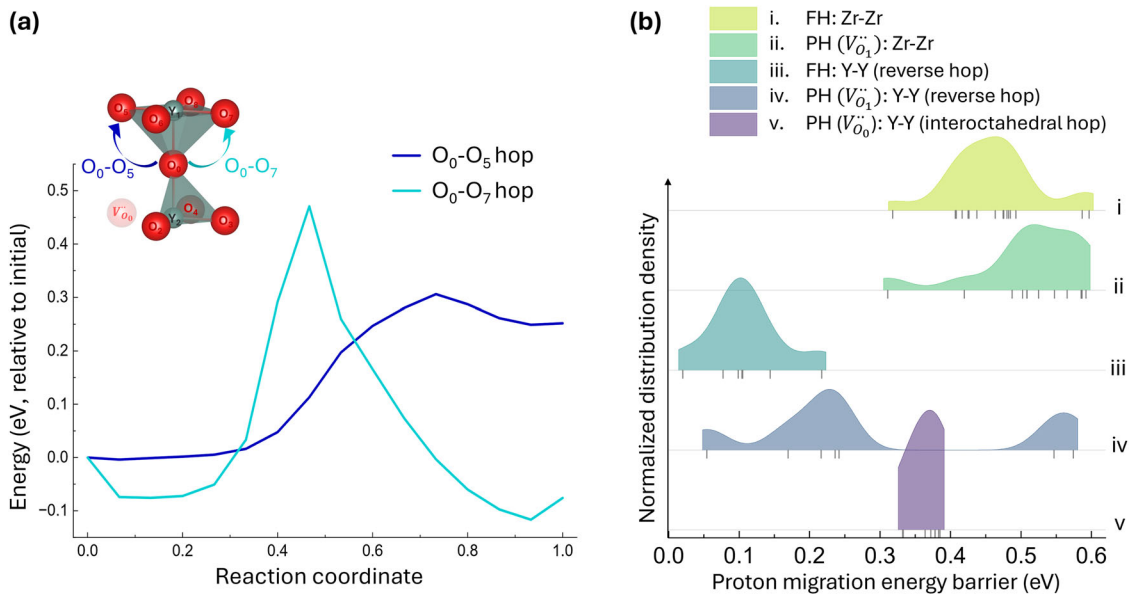

Fig. 4 | Vacancy placement modifies proton migration barriers in partially hydrated Y–Y environments. a Proton migration energy profiles for O_0-O_5 and O_0-O_7 hops in the Y-Y environment with an oxygen vacancy adjacent to a single Y dopant ($V_{O_1}^{\bullet\bullet}$). **b** Distribution curves with rug marks comparing hop-resolved proton migration barriers for FH and PH configurations.

Table 3 | Initial-state structural descriptors and interoctahedral proton migration barriers for vacancy-mediated hops, comparing Zr-Zr and Y-Y local environments

Hop	Zr-Zr environment		Y-Y environment		$\Delta E^{forward}$ (eV)	$\Delta E^{reverse}$ (eV)
	Initial state		Initial state			
	$d_{donor\text{-}acceptor}$ (Å)	$d_{Zr-V_{O_0}^{\bullet\bullet}-Zr}$ (Å)	$d_{donor\text{-}acceptor}$ (Å)	$d_{Y'_{Zr}-V_O^{\cdot}-Y'_{Zr}}$ (Å)		
O_1-O_5	3.113	4.358	2.967	4.274	0.385	0.378
O_2-O_6	3.448	4.382	2.993	4.278	0.378	0.332
O_3-O_7	3.324	4.361	2.974	4.261	0.364	0.383
O_4-O_8	3.824	4.394	3.098	4.252	0.372	0.333
Average	3.427	4.374	3.008	4.266	0.375	0.356

In the Zr-Zr environment, the average donor-acceptor separation in the initial state is 3.43 ± 0.30 Å, while the corresponding Zr − $V_{O_0}^{\bullet\bullet}$ − Zr distance is 4.37 ± 0.02 Å. Here, no stable interoctahedral proton migration pathway was obtained for the Zr-Zr environment. In contrast, in the Y-Y environment, the average separation for interoctahedral hops is reduced to 3.01 ± 0.06 Å, with a $Y'_{Zr} - V_O^{\cdot} - Y'_{Zr}$ distance of 4.27 ± 0.02 Å. Stable migration pathways were obtained for all four interoctahedral hops considered (Table 3), with an average migration barrier of 0.366 ± 0.022 eV. Hop-resolved interoctahedral migration pathways are provided in Supplementary Note S8. Forward and reverse barriers are comparable for all hops, indicating thermodynamically equivalent initial and final states. The hop-resolved migration-barrier distributions for FH and PH configurations are compared in Fig. 4(b), where rug marks indicate the individual calculated barriers used to construct each normalized distribution.

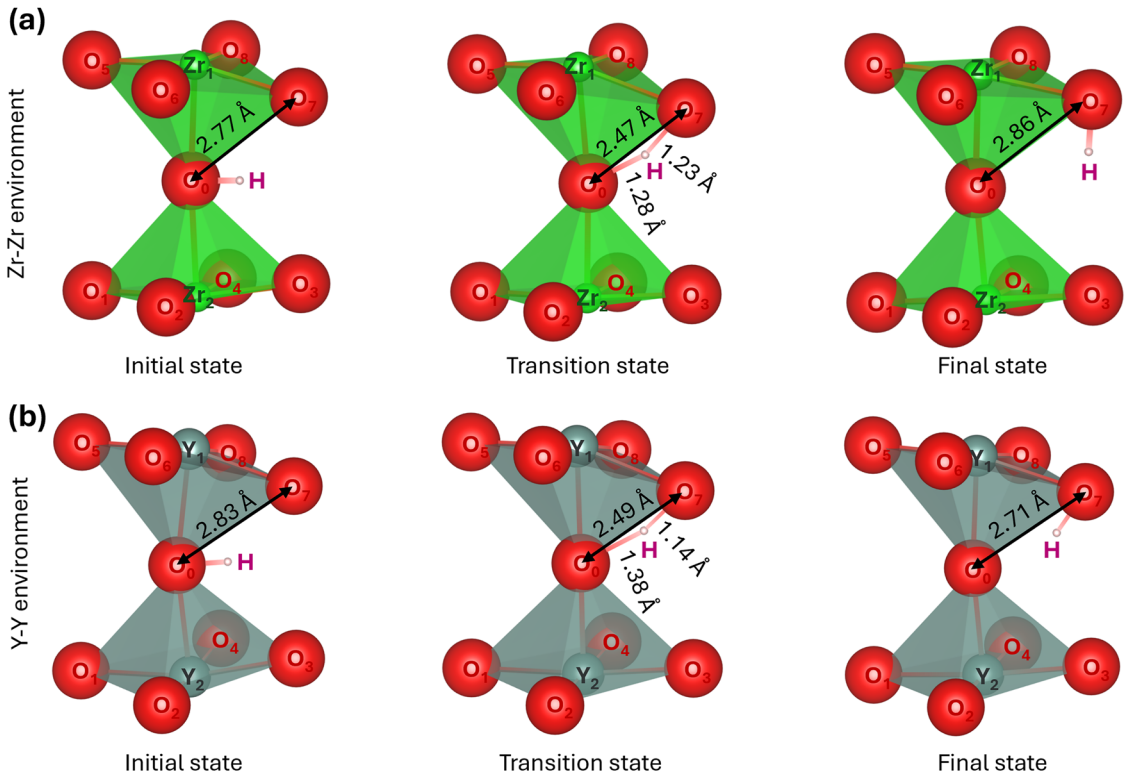

Fig. 5 | Transition-state geometries distinguish symmetric Zr-Zr migration from asymmetric Y-Y trapping in fully hydrated BZY82. Local atomic configurations at the initial state, transition state, and final state for a representative proton hop (O_0-O_7) in the FH lattice: **a** Zr-Zr environment and **b** Y-Y environment.

Discussion

Dopant distributions in BZY introduce spatially heterogeneous elastic and electrostatic fields, leading to configuration-dependent variations in migration-barrier magnitudes. The present analysis focuses on relative mechanistic contrasts between defined coordination environments within a representative dopant realization, rather than on ensemble-averaged transport coefficients. The results are interpreted through topology-driven symmetry breaking and vacancy-modulated transport behavior.

Proton transfer in both Zr-Zr and Y-Y environments proceeds through hydrogen-bond formation at the transition state, accompanied by a reduction in donor-acceptor separation, consistent with prior studies[13,37,44,45] of proton migration in perovskite oxides. However, the nature of the transition state differs noticeably between the two environments. To quantify transition-state proton sharing, an asymmetry parameter was defined as

$$\Delta d_{OH}^{TS} = d_{O_D-H}^{TS} - d_{O_A-H}^{TS} \quad (2)$$

Here, $d_{O_D-H}^{TS}$ and $d_{O_A-H}^{TS}$ are donor-side and acceptor-side O-H distances at the transition state, respectively; therefore, Δd_{OH}^{TS} values from Eq. (2) close to zero indicate nearly symmetric proton sharing at the transition state, whereas Δd_{OH}^{TS} of approximately 0.15–0.30 Å in the present dataset indicate a displacement of the proton toward acceptor oxygen and therefore pronounced transition-state asymmetry.

In the Zr-Zr environment, Δd_{OH}^{TS} remains close to zero for most hops, indicating near-symmetric O-H-O transition states and effective proton sharing between donor and acceptor oxygens. This symmetric transition state is consistent with comparable forward and reverse barriers and nearly degenerate initial and final states. In contrast, the Y-Y environment exhibits systematically positive and larger Δd_{OH}^{TS} values, indicating asymmetric transition states in which the proton is displaced toward the acceptor oxygen. This signed asymmetry is consistent with the thermodynamic bias between initial and final states and the low reverse barriers that promote back-hopping.

Structural analysis of the final configurations reveals a geometric difference between the two environments, as well as transition-state asymmetry. In the Zr-Zr environment (Fig. 5a), the protonated O-H bond lies approximately within the plane defined by the acceptor oxygen and its surrounding Ba coordination. In contrast, in the Y-Y environment (Fig. 5b), the proton remains oriented toward the O_0. This orientation further reduces the transition state geometry for the inverse hop. As a result, the final states remain energetically unfavorable, leading to uniformly small reverse barriers and facilitating facile back-hopping. For the representative Y-Y coordination environment, all eight symmetry-allowed hops originating from O_0 exhibit transition-state asymmetry and thermodynamic bias toward the initial site. O_0 consistently behaves as a proton-trapping site across the symmetry-allowed pathways.

The comparison between oxygen vacancy and hydroxyl migration highlights an asymmetry in the defect transport behavior under PH conditions. The lower migration barriers for hydroxyl diffusion relative to oxygen vacancy diffusion can be attributed to electrostatic effects: hydroxyl defects are locally charge-compensated ($OH_O^{\bullet}$), while oxygen vacancy migration involves a defect with a higher effective charge ($V_{O_0}^{\bullet\bullet}$). Though continuous long-range hydroxyl transport is unlikely, certain symmetry-allowed hops exhibit comparatively lower migration barriers, indicating that localized vehicle-type diffusion can occur under favorable local geometries.

When an oxygen vacancy is coordinated by two Y dopants, the combined negative effective charge of the dopants electrostatically stabilizes the vacancy, favoring the formation of a $Y'_{Zr} - \ddot{V}_O - Y'_{Zr}$ complex. This energetic preference was further confirmed by a relative vacancy-site stability calculation, where the $Y'_{Zr} - \ddot{V}_O - Y'_{Zr}$ configuration was found to be 1.20 eV lower in energy than a vacancy placed far from the Y dopants (Supplementary Note S4). This stabilization is reinforced by local lattice relaxation around the larger Y^{3+} ions, which enhances defect association. The systematic asymmetric diffusion barriers observed for vacancy migration (high barriers for escape and low barriers for recombination in Supplementary Note S5) in all directions provide evidence for this trapping behavior.

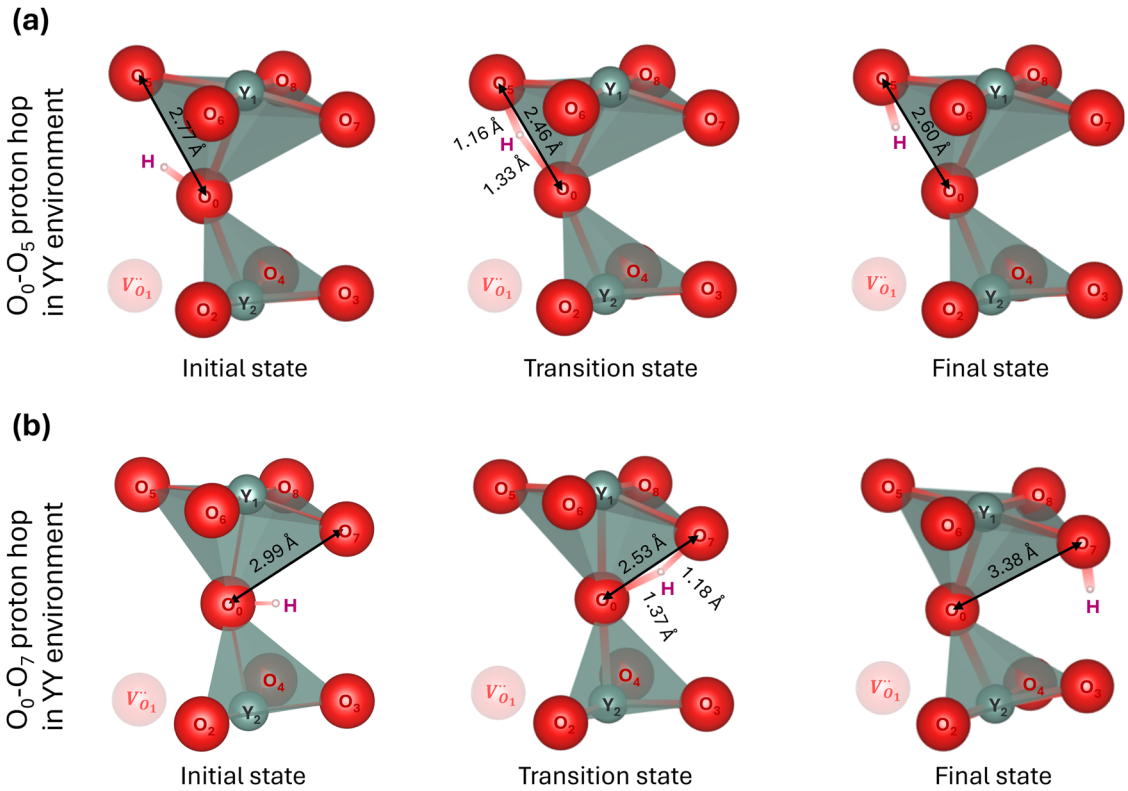

Fig. 6 | An adjacent oxygen vacancy produces pathway-dependent proton migration in partially hydrated Y-Y environments. Initial, transition, and final local geometries for proton migration in PH Y–Y environments with an oxygen vacancy located at the O_1 site. Shown are proton hops from O_0 to (**a**) O_5 and (**b**) O_7. In (**a**), the O–H bond is inclined toward O_5 and away from the vacancy in the initial configuration. In (**b**), the proton does not remain oriented toward the O_0 in the final state.

These results are consistent with previous first-principles studies demonstrating that oxygen vacancies in Y-doped $BaZrO_3$ preferentially associate with Y dopants rather than remaining randomly distributed[32,46,47]. This finding underscores the necessity of explicitly examining proton migration in $Y_{Zr}' - V_O^{\bullet\bullet} - Y_{Zr}'$ configurations, rather than limiting analysis to vacancy-free Y-Y environments where proton trapping dominates, but does not capture vacancy-mediated transport behavior under incomplete hydration conditions.

The introduction of an oxygen vacancy adjacent to a Y-Y environment leads to site-dependent migration behavior. Although transition state asymmetry persists across all Y-Y hops, the degree of proton trapping and the preferred migration pathway depend sensitively on the relative position of the acceptor oxygen with respect to the vacancy.

For the O_0-O_5 hop, the forward migration barrier is substantially reduced to 0.306 eV (Table 2), representing the lowest barrier among all Y-Y hops in the presence of a Y-adjacent vacancy. In an unperturbed configuration, the donor O-H bond adopts a relaxed, approximately planar orientation within the local Ba coordination environment. In the Y-Y environment with a nearby vacancy, this orientation is perturbed: to reduce electrostatic repulsion, the proton shifts away from the positively charged vacancy, tilting the O-H bond away from its planar orientation. When the acceptor oxygen lies opposite the vacancy, this electrostatic bias simultaneously aligns the proton toward the acceptor site, resulting in an inclined O-H orientation toward O_5 and away from the vacancy, as shown in Fig. 6a. This vacancy-induced reorientation lowers the forward migration barrier by stabilizing configurations along the migration coordinate. Despite this reduction, proton trapping persists because both conditions required for trapping are retained: asymmetric transition state ($\Delta d_{OH}^{TS} = 0.253$ Å) and a final-state configuration in which the proton remains oriented towards O_0. Consequently, the reverse barrier remains low, enabling facile back-hopping and maintaining proton trapping behavior similar to that observed in the FH Y-Y environment.

For proton hops to oxygen sites nearest to the vacancy (O_2 and O_4), the transition state asymmetry is modestly reduced relative to other Y-Y hops (Table 2). This reduction leads to a smaller difference between forward and reverse migration barriers compared with the FH case. While proximity to the vacancy partially modifies the transition state geometry, back-hopping is still favored with the trapping effect (Supplementary Note S7.2).

A qualitatively different behavior is observed for proton hops to O_3 and O_7 oxygen sites. These hops exhibit significantly higher reverse barriers (0.574 and 0.547 eV, respectively), indicating an absence of proton trapping essentially. Although the transition-state asymmetry remains comparable to other Y-Y configurations (Table 2 and Fig. 6b), the critical difference arises from the final-state geometry. Unlike typical Y-Y hops, the proton does not remain oriented toward the donor oxygen (O_0) after migration. Instead, relaxation of O_0 toward the vacancy shortens O_3-O_7 separation as shown in Fig. 6b, thereby enabling an alternative interoctahedral migration pathway. Further analysis (Supplementary Note S7.3) demonstrates that proton transfer between O_3 and O_7 is energetically viable, with forward and reverse barriers of 0.355 eV and 0.506 eV, respectively. This pathway competes directly with the reverse O_3 to O_0 and O_7 to O_0 hops, thereby suppressing proton trapping despite the persistence of transition state asymmetry.

An oxygen vacancy positioned between two Y dopants enables interoctahedral proton migration by inducing a local structural environment that is uncommon in Zr-Zr configurations. Although an oxygen vacancy is present in both environments, its effect on proton migration depends critically on the surrounding B-site coordination. In our assessment, the Zr-Zr environment maintains a comparatively large donor-acceptor separation.

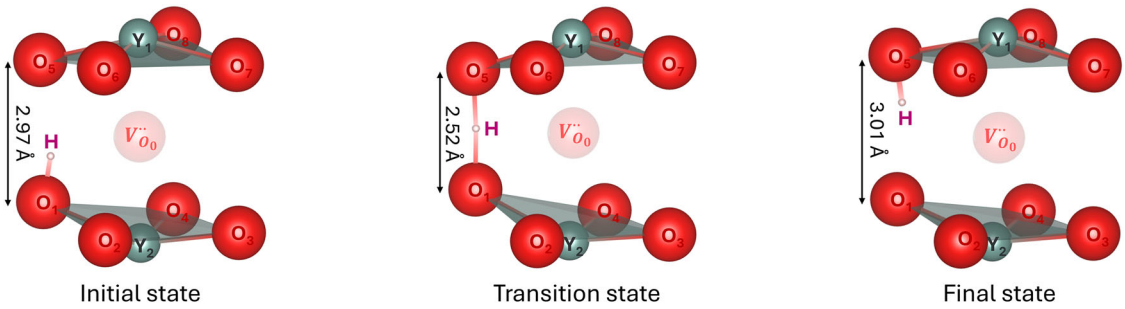

Fig. 7 | A vacancy-centered Y-Y motif enables interoctahedral proton migration in partially hydrated BZY82. Initial, transition, and final local geometries for interoctahedral proton migration from O_1 to O_5 PH Y-Y environments with an oxygen vacancy located at the O_0 site.

Fig. 8 | Vacancy-centered Y-Y coordination transforms excessive proton trapping into trapping-free interoctahedral transport. Fully hydrated Y-Y coordination exhibits excessive proton trapping, while vacancy-centered Y-Y coordination under partial hydration enables lower-barrier interoctahedral proton transport with negligible trapping tendency. The horizontal axis represents the forward migration barrier, and the vertical axis represents trapping tendency estimated from the reverse-to-forward barrier ratio.

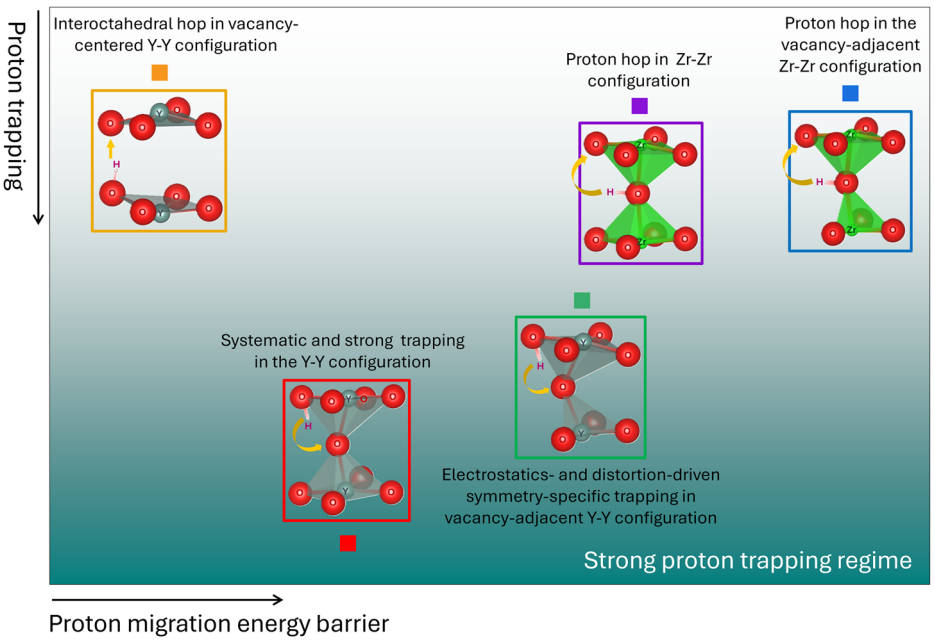

The octahedral tilting that develops along the migration pathway is insufficient to establish a stable hydrogen-bonded configuration, resulting in transient weakening of the O-H bond and preventing the formation of a continuous, energetically viable interoctahedral proton-transfer pathway.

When the vacancy is coordinated by two Y dopants, the surrounding oxygen sites relax toward the vacancy, reducing the initial interoctahedral donor-acceptor separation and enabling further contraction during the transition state through octahedral tilting. As illustrated by representative O_1-O_5 hop (Fig. 7), cooperative lattice distortions enable a stable hydrogen-bonded transition state with a donor-acceptor separation of ≈2.5 Å, comparable to intraoctahedral hops. Equivalent geometric evolution is obtained for all symmetry-related interoctahedral pathways as discussed in Supplementary Note S8.

Under partial hydration, the $Y_{Zr}{}' - V_O^{\bullet\bullet} - Y_{Zr}{}'$ defect complex is thermodynamically favored and therefore expected to form. As hydroxyl migration into this Y-Y coordinated site is also energetically unfavorable, the oxygen site between the two Y dopants is likely to remain vacant, preventing the formation of a stable Y-Y-centered proton site and thereby eliminating trapping. However, this configuration induces cooperative electrostatic stabilization and lattice relaxation that contracts the interoctahedral donor-acceptor separation and enable stable hydrogen-bonded transition states. As a result, all symmetry-allowed interoctahedral hops in this environment exhibit low and nearly symmetric migration barriers that are lower than intraoctahedral proton hops in undoped $BaZrO_3$ and in Zr-Zr environments of BZY82. Consequently, $Y_{Zr}{}' - V_O^{\bullet\bullet} - Y_{Zr}{}'$ complex constitutes a vacancy-enabled, low-barrier interoctahedral proton transport regime. This behavior highlights that proton mobility in PH BZY is governed not only by dopant proximity but by the specific vacancy-dopant topology. The present CI-NEB analysis provides a static energy-landscape description; future molecular dynamics or kinetic Monte Carlo simulations could account for finite-temperature lattice expansion, local structural fluctuations, and their influence on long-range proton diffusivity.

These results show that proton trapping in BZY82 is controlled by both dopant coordination and oxygen-vacancy topology. Under full hydration, the paired-dopant environment produces strong thermodynamic asymmetry and excessive proton trapping, whereas partial hydration changes the local transport landscape by introducing vacancy-mediated electrostatic and structural effects. Most importantly, when the oxygen vacancy occupies the bridging site between the two Y dopants, the resulting vacancy-centered defect associate is stabilized and enables lower-barrier interoctahedral proton migration with negligible trapping tendency. This behavior is summarized schematically in Fig. 8, where the vacancy-centered Y-Y topology shifts proton transport away from the strong-trapping regime. These findings indicate that vacancy placement can suppress conventional dopant-associated trapping and create alternative proton-transfer pathways in partially hydrated Y-doped $BaZrO_3$.

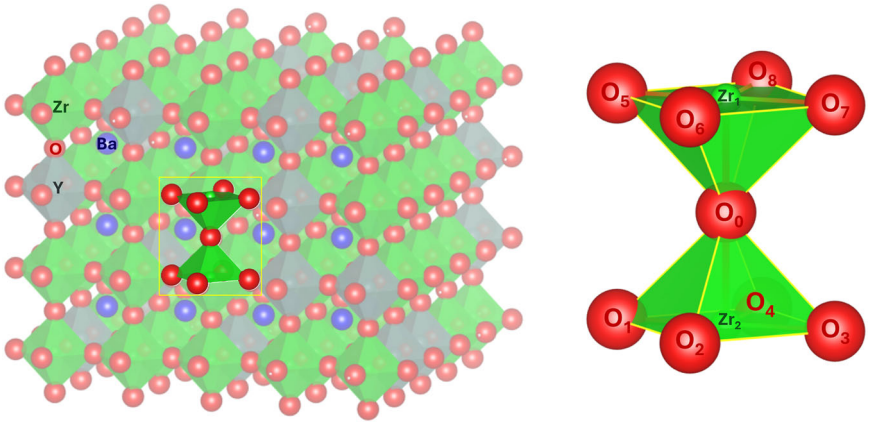

Fig. 9 | The atomistic model defines the local oxygen-network pathways used for defect migration calculations in BZY82. (Left) $5 \times 5 \times 4$ BZY82 supercell highlighting a representative local oxygen coordination environment. (Right) Octahedral connectivity around a donor oxygen site (O_0), showing the eight topologically allowed nearest-neighbor acceptor oxygen sites (O_1-O_8) considered for inter-oxygen migration. Distinct local chemical environments were systematically constructed by controlled modification of neighboring B-site cations (Zr-Zr and Y-Y configurations), oxygen vacancies, and local proton coordination to enable comparative assessment of defect migration pathways.

Methods

Foundation-potential calculations

All atomistic calculations were performed using the charge-equilibrated TensorNet (QET) foundation potential, as implemented in the Materials Graph Library (MatGL)[48,49]. QET is an equivariant, charge-aware foundation potential trained on density-functional-theory (DFT) reference data, incorporating an analytically solvable linear-scaling charge-equilibration scheme to account for non-local electrostatic interactions[50]. Atomic structures were processed using the Atomic Simulation Environment (ASE) together with the pymatgen-ASE interface[51,52]. In the present work, the pretrained QET-MatQ model was employed to evaluate total energies and atomic forces for geometry optimization and transition-state sampling.

Supercell and defect configurations

A cubic $BaZrO_3$ perovskite unit cell with a lattice parameter of 4.21 Å was replicated $5 \times 5 \times 4$ to construct the simulation supercell. Y-doped $BaZrO_3$ with a nominal composition of $Ba(Zr_{0.8}Y_{0.2})O_{3-\delta}$ (BZY82) was generated by random substitution of 20% of Zr sites with Y. In the FH configuration, 20 H atoms were added to randomly selected oxygen sites to compensate for the 20 Y acceptor dopants, with each oxygen allowed to host at most one H. In the PH configuration, oxygen vacancies were introduced to obtain 50% nominal hydration, such that half of the acceptor dopants were compensated by protons and the remaining charge compensation was provided by oxygen vacancies. These initial defect placements were random and charge-neutral. Controlled local defect configurations were then constructed for the proton migration analyses. In the FH case, proton migration was examined in vacancy-free Zr-Zr, Y-Y local environments to assess dopant-associated effects on proton trapping. In the PH case, vacancy positions and proton orientations were modified near selected local environments, while keeping the remaining atomic arrangement unchanged, to evaluate how vacancy placement affects proton migration, oxygen-vacancy migration, and hydroxyl migration. This procedure allowed us to separate the effect of random initial defect placement from the controlled vacancy-dopant topologies used for mechanistic comparison.

Local structural distortion analysis

Local structural distortion was evaluated from fully relaxed configurations under periodic boundary conditions, with forces converged below 0.01 eV $Å^{-1}$. To obtain a statistically reliable characterization of heterogeneous defect environments, distortion analysis was performed in an expanded $10 \times 10 \times 8$ supercell containing 2400 oxygen sites, minimizing finite-size effects and improving sampling of local chemical variability. Distortion was quantified from the displacement of each oxygen atom relative to its ideal lattice position after optimal alignment. Oxygen environments were classified based on Y-dopant coordination, where sites coordinated by two Y cations within the first-nearest-neighbor shell were assigned to the Y-Y environment and extended to nearby oxygen sites to capture the spatial extent of dopant-induced lattice distortion. Zr-Zr environments were identified by excluding oxygen sites with nearby Y dopants, and B-O-B bond angles were evaluated to characterize local octahedral distortion.

Migration-barrier calculations

The protonated structures were fully relaxed until the maximum residual force on any atom was below 0.02 eV $Å^{-1}$, ensuring convergence of local structural relaxations associated with proton binding. The migration barriers were evaluated using the climbing-image nudged-elastic band (CI-NEB) method[53]. For each selected donor oxygen site, migration barriers were computed for all eight topologically allowed nearest-neighbor hopping pathways defined by the octahedral connectivity of the perovskite lattice (Fig. 9). Minimum-energy paths were resolved using 16 replicas, and all NEB calculations were converged to a force tolerance of 0.02 eV $Å^{-1}$. Migration barriers were defined as the energy difference between the transition state and the fully relaxed initial configuration, with energies referenced to the initial state. For PH configurations, migration of protons, oxygen vacancies, and hydroxyl defects was explicitly examined across distinct local chemical environments. All hop-resolved analyses were performed for a representative random dopant realization and a selected donor oxygen site chosen to represent Zr-Zr and Y-Y nearest B-site coordination environments. While quantitative barrier values depend on the specific dopant arrangement and local strain field, the objective here is to isolate mechanistic differences between vacancy-free and vacancy-mediated coordination motifs under controlled local chemistries. Crystal structures and coordination polyhedra were visualized using the VESTA software package[54].

Data availability

The datasets generated and/or analyzed during the current study are not publicly available because they are part of ongoing related research and include large raw and intermediate atomistic simulation files, but are available from the corresponding author on reasonable request.

Code availability

The custom Python scripts used for structure generation, defect-configuration construction, CI-NEB setup, migration-barrier extraction, and data analysis are not publicly available because they are part of ongoing related research, but are available from the corresponding author on reasonable request. The calculations were performed using the Atomic Simulation Environment, pymatgen-ASE interface, Materials Graph Library, and the QET-MatQ-PES foundation potential. The relevant simulation settings, including supercell size, hydration state, relaxation criteria, and force-convergence thresholds, are provided in the Methods section.

Received: 10 March 2026; Accepted: 24 June 2026;
Published online: 07 September 2026

References

1. Ding, H. et al. Self-sustainable protonic ceramic electrochemical cells using a triple conducting electrode for hydrogen and power production. *Nat. Commun.* **11**, 1907 (2020).
2. Zhou, Y. et al. Strongly correlated perovskite fuel cells. *Nature* **534**, 231–234 (2016).
3. Gao, R. et al. Designing optimal perovskite structure for high ionic conduction. *Adv. Mater.* **32**, e1905178 (2020).
4. Luo, Z. et al. First observation of electrode-correlated protonic conductivity of perovskite-type electrolytes and way towards optimization. *Energy Environ. Sci.* **17**, 4115–4125 (2024).
5. Patel, S. et al. Orientation microscopy–assisted grain boundary analysis for protonic ceramic cell electrolytes. *J. Am. Ceram. Soc.* **108**, e20371 (2025).
6. Han, D. & Uda, T. The best composition of an Y-doped $BaZrO_3$ electrolyte: selection criteria from transport properties, microstructure, and phase behavior. *J. Mater. Chem. A* **6**, 18571–18582 (2018).
7. Bae, K. et al. Demonstrating the potential of yttrium-doped barium zirconate electrolyte for high-performance fuel cells. *Nat. Commun.* **8**, 14553 (2017).
8. Zheng, S. et al. Interfacial nanostructuring enables integrated, low-polarization reversible protonic ceramic cells. *Adv. Energy Mater* **16**, e70850 (2026).
9. Patel, S., Liu, F., Ding, H., Duan, C. & Ghamarian, I. On proton conduction mechanism for electrolyte materials in solid oxide fuel cells. *Int.l J. Hydrogen Energy* **72**, 1236–1248 (2023).
10. Bello, I. T. et al. Multiscale engineering of $BaZr_{1-x}Y_xO_{3-\delta}$-based protonic ceramics: a critical review of defect chemistry, interface design, and computational insights. *Energy Rev.* **4**, 100165 (2025).
11. Zheng, S. et al. Hybridizing electrode interface structures in protonic ceramic cells for durable, reversible hydrogen and power generation. *Adv. Mater.* 2503649 (2025).
12. Patel, S. et al. in *Electrochemical Society Meeting Abstracts 248*, 2301–2301 (The Electrochemical Society, Inc.) (2025).
13. Torayev, A. et al. Local distortions and dynamics in hydrated Y-doped $BaZrO_3$. *J. Phys. Chem. C.* **124**, 16689–16701 (2020).
14. Draber, F. M. et al. Nanoscale percolation in doped $BaZrO_3$ for high proton mobility. *Nat. Mater.* **19**, 338–346 (2020).
15. Yamazaki, Y. et al. Proton trapping in yttrium-doped barium zirconate. *Nat. Mater.* **12**, 647–651 (2013).
16. Cao, J., Ji, Y. & Shao, Z. Perovskites for protonic ceramic fuel cells: a review. *Energy Environ. Sci.* **15**, 2200–2232 (2022).
17. Kasamatsu, S., Sugino, O., Ogawa, T. & Kuwabara, A. Dopant arrangements in Y-doped $BaZrO_3$ under processing conditions and their impact on proton conduction: a large-scale first-principles thermodynamics study. *J. Mater. Chem. A* **8**, 12674–12686 (2020).
18. Kreuer, K. D. Proton-Conducting Oxides. *Annu. Rev. Mater. Res.* **33**, 333–359 (2003).
19. Kreuer, K.-D., Paddison, S. J., Spohr, E. & Schuster, M. Transport in proton conductors for fuel-cell applications: simulations, elementary reactions, and phenomenology. *Chem. Rev.* **104**, 4637–4678 (2004).
20. Norby, T., Widerøe, M., Glöckner, R. & Larring, Y. Hydrogen in oxides. *Dalton Trans.* **19**, 3012–3018 (2004).
21. Zheng, S. et al. Vacancy–redox coupling at interface-engineered heterostructures enhances reversible energy conversion in protonic ceramic cells. *Angew. Chem. Int. Ed.* **138**, e7079252 (2026).
22. Yamazaki, Y., Babilo, P. & Haile, S. M. Defect chemistry of yttrium-doped barium zirconate: a thermodynamic analysis of water uptake. *Chem. Mater.* **20**, 6352–6357 (2008).
23. Bjørheim, T. S., Kotomin, E. A. & Maier, J. Hydration entropy of $BaZrO_3$ from first principles phonon calculations. *J. Mater. Chem. A* **3**, 7639–7648 (2015).
24. Vera, C. Y. R. et al. A mini-review on proton conduction of $BaZrO_3$-based perovskite electrolytes. *J. Phys.: Energy* **3**, 032019 (2021).
25. Dawson, J. A., Miller, J. A. & Tanaka, I. First-principles insight into the hydration ability and proton conduction of the solid state proton conductor, Y and Sn Co-Doped $BaZrO_3$. *Chem. Mater.* **27**, 901–908 (2015).
26. Joos, M., Kang, X., Merkle, R. & Maier, J. Water uptake of solids and its impact on ion transport. *Nat. Mater.* **24**, 821–834 (2025).
27. Fluri, A. et al. Enhanced proton conductivity in Y-doped $BaZrO_3$ via strain engineering. *Adv. Sci.* **4**, 1700467 (2017).
28. Takahashi, H. et al. First-principles calculations for the energetics of the hydration reaction of acceptor-doped BaZrO3. *Chem. Mater.* **29**, 1518–1526 (2017).
29. Regalado Vera, C. Y. et al. Improving proton conductivity by navigating proton trapping in high scandium-doped barium zirconate electrolytes. *Chem. Mater.* **35**, 5341–5352 (2023).
30. Toyoura, K., Meng, W., Han, D. & Uda, T. Preferential proton conduction along a three-dimensional dopant network in yttrium-doped barium zirconate: a first-principles study. *J. Mater. Chem. A* **6**, 22721–22730 (2018).
31. Ding, J. et al. The influence of local distortions on proton mobility in acceptor doped perovskites. *Chem. Mater.* **30**, 4919–4925 (2018).
32. Kasamatsu, S., Sugino, O., Ogawa, T. & Kuwabara, A. Dopant arrangements in Y-doped BaZrO3 under processing conditions and their impact on proton conduction: a large-scale first-principles thermodynamics study. J. Mater. Chem. A 8 (25): 12674–12686 (2020).
33. Yamazaki, Y. et al. Oxygen affinity: the missing link enabling prediction of proton conductivities in doped barium zirconates. *Chem. Mater.* **32**, 7292–7300 (2020).
34. Urban-Klaehn, J. et al. Hydrated doped-$BaZrO_3$ proton conductors studied by positron annihilation lifetime spectroscopy. *Solid State Ion.* **402**, 116365 (2023).
35. Rowberg, A. J., Li, M., Ogitsu, T. & Varley, J. B. Incorporation of protons and hydroxide species in $BaZrO_3$ and $BaCeO_3$. *Mater. Adv.* **4**, 6233–6243 (2023).
36. Draber, F. M., Denninger, J. R., Müller, P. C., Sommerfeld, I. K. & Martin, M. The impact of nanoscale percolation in yttrium-doped $BaZrO_3$ on the oxygen ion and proton conductivities: a density functional theory and kinetic Monte Carlo study. *Adv. Energy Sustain. Res.* **3**, 2200007 (2022).
37. Merinov, B. & Goddard, W. Proton diffusion pathways and rates in Y-doped $BaZrO_3$ solid oxide electrolyte from quantum mechanics. *J. Chem. Phys.* **130**, 194707 (2009).
38. Raiteri, P., Gale, J. D. & Bussi, G. Reactive force field simulation of proton diffusion in BaZrO3 using an empirical valence bond approach. *J. Phys.: Condens. Matter* **23**, 334213 (2011).
39. Stokes, S. J. & Islam, M. S. Defect chemistry and proton-dopant association in $BaZrO_3$ and $BaPrO_3$. *J. Mater. Chem.* **20**, 6258–6264 (2010).
40. Gu, J., Jiang, L., Ismail, S. A., Guo, H. & Han, D. Surface protonic conduction on oxide ceramics: mechanism, materials, and method for characterization. *Adv. Mater. Interfaces* **10**, 2201764 (2023).
41. Pasierb, P., Wierzbicka, M., Komornicki, S. & Rekas, M. Structural, electrical and transport properties of yttrium-doped proton-conducting strontium cerates. *J. power sources* **173**, 681–687 (2007).
42. Zou, P. et al. A fast ceramic mixed OH^-/H^+ ionic conductor for low temperature fuel cells. *Nat. Commun.* **15**, 909 (2024).
43. Jiang, S., Shu, X., Zheng, X., Pan, H. & Sun, W. Ba (Zr, Ce) O_3-based proton-conducting solid oxide electrolysis cells for efficient hydrogen production. *J. Mater. Chem. A* **13**, 41429–41442 (2025).

44. Gomez, M. A. et al. The effect of yttrium dopant on the proton conduction pathways of $BaZrO_3$, a cubic perovskite. *J. Chem. Phys.* **132**, 214709 (2010).
45. Chung, H. W., Žguns, P., Li, J. & Yildiz, B. Flexibility of oxygen sublattice and hydrogen bond length predict proton mobility in ternary metal oxides. *Matter* **9**, 102568 (2025).
46. Lin, Z. et al. Oxygen vacancies altering the trapping in the proton conduction landscape of doped barium zirconate. *J. Phys. Chem. C.* **124**, 27954–27964 (2020).
47. Eisele, S., Draber, F. M. & Grieshammer, S. The effect of ionic defect interactions on the hydration of yttrium-doped barium zirconate. *Phys. Chem. Chem. Phys.* **23**, 4882–4891 (2021).
48. Ko, T. W. et al. Materials Graph Library (MatGL), an open-source graph deep learning library for materials science and chemistry. *npj Comput. Mater.* **11**, 253 (2025).
49. Wang, M. et al. Deep graph library: a graph-centric, highly-performant package for graph neural networks. *arXiv preprint* arXiv: https://arxiv.org/abs/1909.01315 (2019).
50. Ko, T. W., Liu, R., Mishra, A. R. & Yu, Z. A fast, accurate, and reactive equivariant foundation potential. *arXiv preprint* arXiv: https://arxiv.org/abs/2511.07249 (2025).
51. Larsen, A. H. et al. The atomic simulation environment—a Python library for working with atoms. *J. Phys.: Condens. Matter* **29**, 273002 (2017).
52. Ong, S. P. et al. Python Materials Genomics (pymatgen): a robust, open-source python library for materials analysis. *Comput. Mater. Sci.* **68**, 314–319 (2013).
53. Henkelman, G., Uberuaga, B. P. & Jónsson, H. A climbing image nudged elastic band method for finding saddle points and minimum energy paths. *J. Chem. Phys.* **113**, 9901–9904 (2000).
54. Momma, K. & Izumi, F. VESTA 3 for three-dimensional visualization of crystal, volumetric and morphology data. *Appl. Crystallogr.* **44**, 1272–1276 (2011).

Acknowledgements

S.P. acknowledges the support of the U.S. National Science Foundation under the Accelerating Research Translation program 2331409. I.G. acknowledges the Research Council of the University of Oklahoma and the Samuel Roberts Noble Microscopy Laboratory at the University of Oklahoma.

Author contributions

S.P. contributed to the conceptualization, methodology, visualization, primary investigation, analysis, and writing of the original draft. I.G. contributed to conceptualization, supervision, analysis, funding acquisition, reviewing, and editing the draft. S.X. contributed to methodology, analysis, reviewing, and editing the draft. A.N. contributed to methodology, reviewing, and editing the draft. J.L., S.Z., D.C., H.D., P.K., F.L., and Y.L. contributed to reviewing and editing the draft.

Competing interests

The authors declare no competing interests.

Additional information

Supplementary information The online version contains supplementary material available at https://doi.org/10.1038/s44456-026-00013-5.

Correspondence and requests for materials should be addressed to Iman Ghamarian.